Available online at www.sciencedirect.com
SCIENCE DIRECT
Acta Materialia 54 (2006) 2489–2499
Acta MATERIALIA
www.actamat-journals.com

Nanodisturbances in deformed Gum Metal

Mikhail Yu. Gutkin [a,*], Toshitaka Ishizaki [b], Shigeru Kuramoto [b], Ilya A. Ovid'ko [a]

[a] Institute of Problems of Mechanical Engineering, Russian Academy of Sciences, Bolshoj 61, Vas. Ostrov, St. Petersburg 199178, Russian Federation
[b] Toyota Central Research and Development Laboratories Incorporated, Nagakute Aichi, 480-1192, Japan

Received 22 December 2005; received in revised form 18 January 2006; accepted 23 January 2006
Available online 20 March 2006

Abstract

Systematic experiments have been performed to characterize defect structures in deformed Gum Metal, a special titanium alloy with high strength, low Young's modulus, excellent cold workability and low resistance to shear in certain crystallographic planes. Results from high-resolution transmission electron microscopy characterization reveal nanodisturbances (planar nanoscopic areas of local shear) as typical elements of defect structures in deformed Gum Metal. A theoretical model is suggested describing nanodisturbances as nanoscale dipoles of non-conventional partial dislocations with arbitrary, non-quantized Burgers vectors. It is shown theoretically that the homogeneous generation of nanodisturbances is energetically favorable in Gum Metal, where they effectively carry plastic flow.

Keywords: Titanium alloys; Deformation; Dislocations; Nanostructures

1. Introduction

Recently, Saito et al. developed a new multi-functional β-titanium alloy with high strength, low Young's modulus and excellent cold workability [1,2]. This alloy, Gum Metal, is composed of group Va additional elements, such as Ta, Nb and V, group IVa additional elements, such as Zr and Hf, a small amount of oxygen, and the balance Ti. Further, the chemical composition is characterized by three electronic magic numbers: (i) a valence electron number (e/a) of 4.24; (ii) a bond order (Bo value) based on the DV-Xα method of 2.87; (iii) an electron orbital energy level (Md value) of 2.45. Typical compositions of Gum Metal which fulfill the above conditions are described as follows: Ti–12Ta–9Nb–3V–6Zr–1.2O, Ti–23Nb–0.7Ta–2Zr–1.2O and Ti–20Nb–3.5Ta–3.4Zr–1.2O (at.%). It is important that the unique properties of the alloy appear after substantial cold working; indeed, one of the remarkable properties of Gum Metal is its excellent cold workability. The alloy shows much less work hardening than ordinary metals even up to a reduction in area of 90%. Such cold workability can be related to the unique deformation mechanism of the alloy [3].

Saito et al. observed the lattice image after cold swaging by 90%, obtained using high-resolution transmission electron microscopy (HRTEM) with an electron beam direction parallel to $\langle 1\,1\,0\rangle$ [1,2]. It was shown that concentrated lattice disturbances of a nanometer scale were distributed along $\langle 1\,1\,1\rangle\{1\,1\,2\}$, while there were few mobile dislocations. These nanodisturbances were different from the usual dislocations because their slip displacement along $\langle 1\,1\,1\rangle\{1\,1\,2\}$ was much smaller than the lattice spacing of $\{1\,1\,1\}$. It was also observed at the macroscale that unique faults were formed in Gum Metal during plastic deformation. The deformation structure exhibited giant planar faults after tensile deformation by 10% [1,2]. It was confirmed by crystal orientation analysis that these giant faults were formed almost along a plane in a direction orientated 45° from the tensile direction, but were not completely parallel to each other. It was also confirmed that there was a vast amount of strain accumulation in the vicinity of the giant faults, which was characterized by a crystallographic rotation of 20–30° from the neighboring area.

* Corresponding author.
E-mail address: gutkin@def.ipme.ru (M.Yu. Gutkin).

1359-6454/$30.00
doi:10.1016/j.actamat.2006.01.027

It has been noted that the ideal shear stress of the alloy can be estimated as approximately equal to the actual strength [1–3]. Usually, the ideal strength for most metals is several tens of times larger than the actual strength, and it is considered that dislocation activity plays an important role in plastic deformation with a much lower stress than the ideal shear stress. In contrast, it has been implied that the deformation process from the ideal shear can proceed due to the much lower ideal strength in the case of Gum Metal [3]. Previous results indicated the existence of nanodisturbances and the formation of giant faults in Gum Metal. It is considered that nanodisturbances can be formed under the specific condition that plastic deformation proceeds by ideal shear. Therefore, the deformation process with nanodisturbances is an interesting focus for revealing this unique deformation mechanism, but an explicit explanation of the deformation process remains to be elucidated. In the present paper these nanodisturbances are investigated using HRTEM to examine the deformation mechanism. The validity of the presence of nanodisturbances is examined by theoretical analysis and the reason why the generation of nanodisturbances prevails over usual dislocations is discussed. Also, in the concluding section, the notion of nanodisturbances is briefly considered as useful in a description of enhanced intergrain sliding in nanocrystalline materials showing ductility and superplasticity.

2. Elastically softened directions and low ideal strengths expected from calculations

In a previous paper, calculation analysis based on first principles with the ultrasoft pseudo-potential method indicated that Gum Metal has a unique elastic anomaly with several elastically softened directions [4]. According to the analysis of elastic constants of body-centered cubic (bcc) Ti–X (X = Nb, Ta, V, Mo) binary alloys with varying valence electron number e/a, the subtraction of two elastic constants, c_{11}–c_{12}, is nearly equal to 0 around an e/a of 4.24. The same elastic anomaly occurs in Gum Metal because its e/a is approximately 4.24.

Young's moduli and shear moduli along some orientations in monocrystals and polycrystals can be estimated from the elastic constants c_{11}, c_{12} and c_{44} using the formula in Table 1. If c_{11}–c_{12} is nearly equal to 0, a tensile elastic modulus of $\langle 100\rangle$(E_{100}) and shear elastic moduli of $\langle 110\rangle\{110\}$ and $\langle 111\rangle\{110\}$, $\{112\}$ or $\{123\}$ (G_{110} and G_{111}) of the alloy would be nearly equal to 0 simultaneously. Ideal strengths can also be estimated to be very small from elastic constants. In the case of bcc metals, the ideal strengths for tensile separation of $\{001\}$, σ_{max}, and for shear along $\langle 111\rangle\{110\}$, $\{112\}$ or $\{123\}$, τ_{max}, are given by the following approximations [5]: $\sigma_{max} \approx 0.083 E_{100}$ and $\tau_{max} \approx 0.11 G_{111}$. Therefore, Gum Metal can attain very small ideal strengths from the elastic anomaly.

3. Experimental observations of nanodisturbances

3.1. Experimental

To investigate nanodisturbances, we employed the following specimens: Gum Metal specimen (Ti–20Nb–3.5Ta–3.4Zr–1.2O) swaged by 90%, Gum Metal specimens rolled by 1% and 10%, and a β-Ti alloy specimen (Ti–14V–5.4Al–2.8Cr–1.2Sn) rolled by 1% which is a reference for comparison of phase stability between Gum Metal and a conventional β-Ti alloy. The valence electron numbers e/a of the Gum Metal specimens and the β-Ti alloy specimen are 4.24 and 4.14, respectively. Every specimen was cold worked after solution heat treatment for 30 min at 900 °C. The swaged specimen was used to investigate details in the deformation structure after severe cold working, while the rolled specimens were used to study the deformation structure at an early stage of plastic deformation.

The specimens for TEM observation were prepared using the focused ion beam (FIB) method. HRTEM observation was carried out on the swaged Gum Metal specimen

Table 1
Young's and shear moduli of each direction for bcc metals

	Young's moduli	Shear moduli
Monocrystal	$\langle 001\rangle$ Tension	Along $\langle 001\rangle$ on $\{010\}$
	$E_{001} = \frac{(c_{11}-c_{12})(c_{11}+2c_{12})}{c_{11}+c_{12}}$	$G_{001} = c_{44}$
	$\langle 011\rangle$ Tension	Along $\langle 011\rangle$ on $\{011\}$
	$E_{011} = \left\{\frac{c_{11}+c_{12}}{(c_{11}+2c_{12})(c_{11}-c_{12})} + \frac{1}{4}\left(\frac{1}{c_{44}} - \frac{2}{c_{11}-c_{12}}\right)\right\}^{-1}$	$G_{011} = \frac{c_{11}-c_{12}}{2}$
	$\langle 111\rangle$ Tension	Along $\langle 111\rangle$ on $\{011\}\{112\}\{123\}$
	$E_{111} = \left\{\frac{c_{11}+c_{12}}{(c_{11}+2c_{12})(c_{11}-c_{12})} + \frac{1}{3}\left(\frac{1}{c_{44}} - \frac{2}{c_{11}-c_{12}}\right)\right\}^{-1}$	$G_{111} = \frac{3c_{44}(c_{11}-c_{12})}{c_{11}-c_{12}+4c_{44}}$
Polycrystal	$E = \frac{(c_{11}-c_{12}+3c_{44})(c_{11}+2c_{12})}{2c_{11}+3c_{12}+c_{44}}$	$G = \frac{c_{11}-c_{12}+3c_{44}}{5}$

using a JEM-ARM1250 instrument (JEOL) with an acceleration voltage of 1250 kV. To compare deformation structures between the rolled Gum Metal and the β-Ti alloy specimens, lattice images were obtained using a H-9000NAR instrument (Hitachi) with an acceleration voltage of 300 kV. Observations around giant faults in the Gum Metal specimen rolled by 10% were also carried out using a JEM 2010FEF instrument (JEOL) with an acceleration voltage of 200 kV for a detailed characterization of nanosize faults near giant faults.

3.2. Results

Fig. 1 shows lattice images of the Gum Metal specimen swaged by 90%. Several lattice images were taken to reveal differences in lattice structures among the observation areas. While the outline of a defect structure after severe plastic deformation has been introduced in previous papers [1,2], detailed features of faults can be explained by these new images. It is obvious that there are differences in the amount of local structural change depending on the observation area. There is no distorted lattice arrangement in image (a), which signifies very little strain localization in this observation area, while other images show clear localized distortion in the lattice arrangements compared to image (a). Images (b) and (c) show local disarrangement in (1 1 0) planes that is made by the shear along $\langle 1\,1\,1\rangle\{1\,1\,2\}$, one of the elastically softened directions of Gum Metal. Images (d) and (e) show more significantly distorted areas with larger local strains than those of images (b) and (c); here the shear direction is also $\langle 1\,1\,1\rangle\{1\,1\,2\}$. It can also be seen that the sizes of the local shears in these images are restricted to the nanoscale.

Cross-sectional observations for the β-Ti alloy specimen rolled by 1% and the Gum Metal specimens rolled by 1% and 10% were made to investigate structures around giant faults. These images are shown in Fig. 2. Figs. 2(b) and (c) indicate that there are some giant faults that divide the

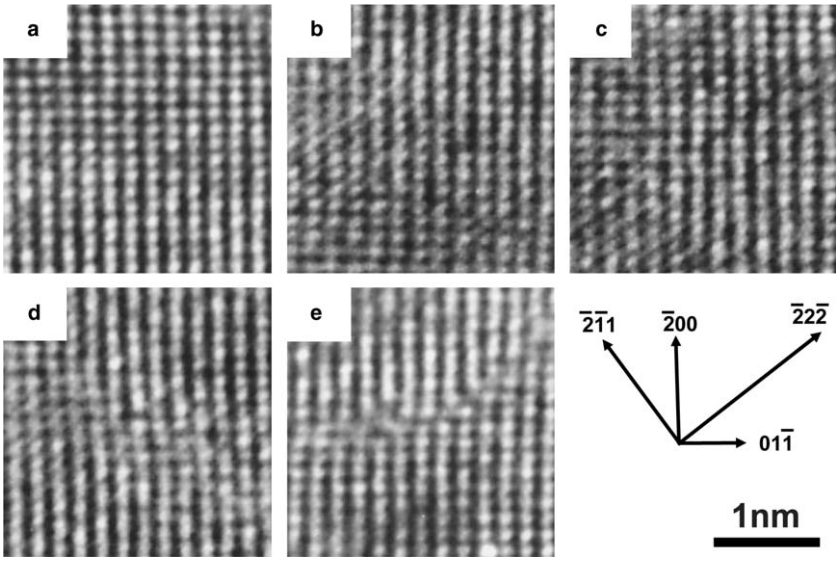

Fig. 1. High-resolution lattice images of the Gum Metal specimen swaged by 90% with an electron beam direction parallel to $\langle 1\,1\,0\rangle$. The images reveal differences among the observation areas.

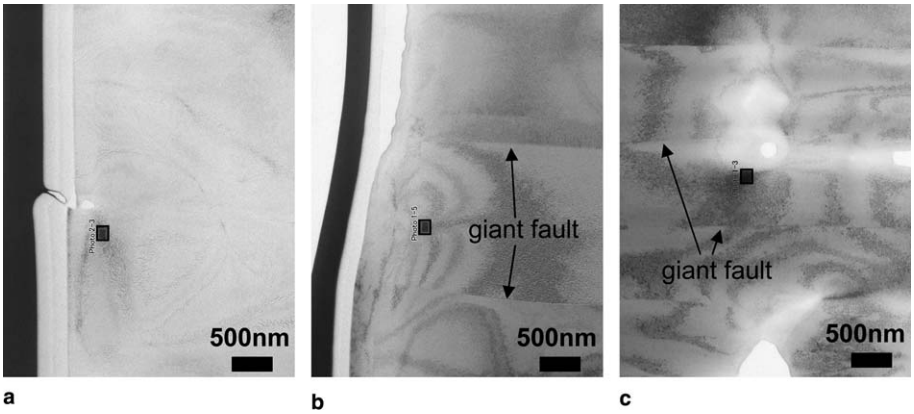

Fig. 2. TEM images of the cross-sectional observations for the β-Ti alloy specimen rolled by 1% (a) and the Gum Metal specimens rolled by 1% (b) and 10% (c). The rectangular regions marked in each image indicate the observation place for the lattice image taken at low resolution in Fig. 3.

initial grain into subgrains. Fig. 3 shows comparisons of low-resolution images of the rolled specimens; images taken at designated rectangular regions in Fig. 2. It can be seen that the Gum Metal specimens show areas with distorted lattice arrangements compared with the β-Ti alloy; local changes in black and white contrast are more frequently observed in the Gum Metal specimens. Because the contrast changes correspond to local changes in crystal orientation, the deformation structure in Gum Metal has a very inhomogeneous distribution of strain even after the 1% deformation. The inhomogeneous distribution of strain becomes more localized by the progress of plastic deformation, as shown for the 10% rolled specimen.

We compared the lattice arrangement of the β-Ti alloy specimen rolled by 1% with those of the Gum Metal specimens rolled by 1% and 10% from high-resolution lattice images as shown in Fig. 4. The image of the β-Ti alloy specimen (Fig. 4(a)) includes no local disarrangement after rolling by 1%, while that of the Gum Metal specimen (Fig. 4(b)) includes distortion of the lattice arrangement at the same amount of deformation. Similar distortions of the lattice arrangement are also seen in the images of the Gum Metal specimen rolled by 10%, as shown in Figs. 4(c)–(e). There are also significant differences in the magnitudes of the distortion of the lattice arrangements among the images in Figs. 4(c)–(e). This feature is the same as that for the deformed structure shown in Fig. 1, which revealed inhomogeneous distributions of distortions depending on the observation area. Since the direction of the electron beam is parallel to ⟨1 1 1⟩, the images show local disarrangement in (1 1 0) planes. They look similar to the images containing nanodisturbances in the swaged specimen, in which the nanodisturbances were formed along the elastically softened directions.

Fig. 5 shows the observation area for a giant fault in the Gum Metal specimen rolled by 10%. The image shows an area in the vicinity of the giant fault, which was thinned by a FIB to obtain a lattice image. The lattice image of

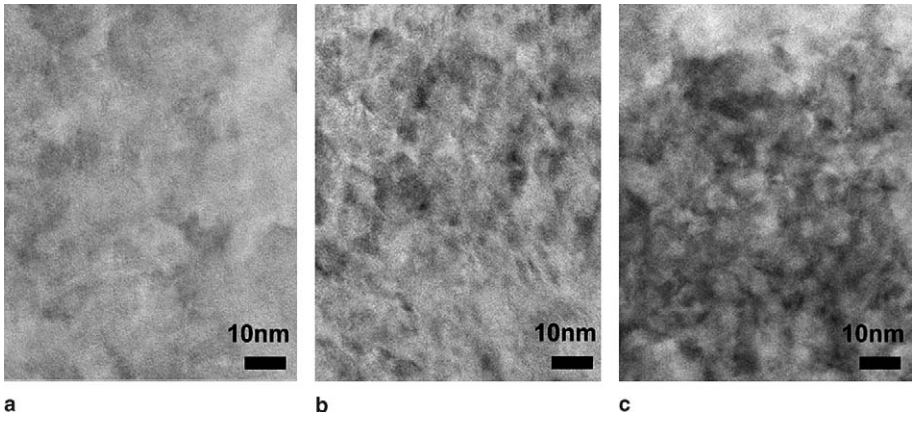

Fig. 3. Comparisons of low-resolution lattice images of a β-Ti alloy specimen rolled by 1% (a) and Gum Metal specimens rolled by 1% (b) and 10% (c). Each image was taken at the rectangular region designated in Fig. 2 with an electron beam direction parallel to ⟨1 1 1⟩.

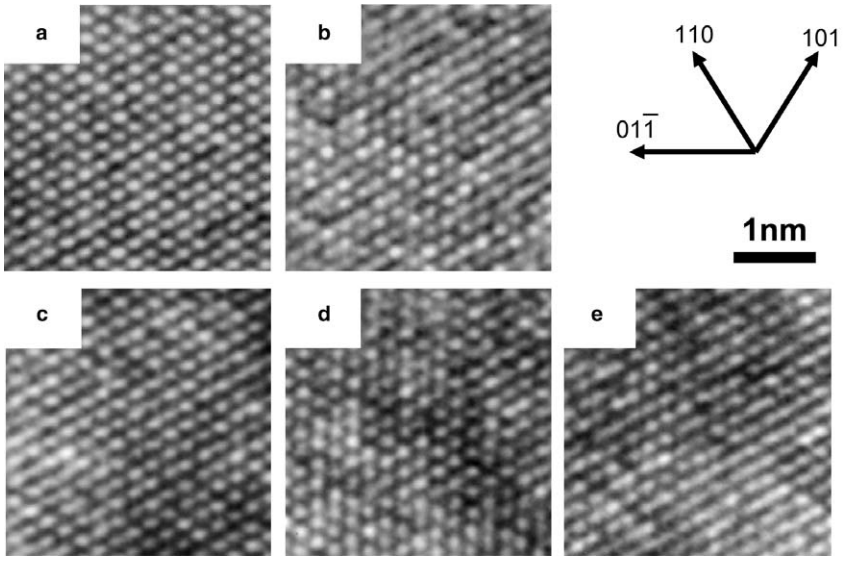

Fig. 4. High-resolution lattice images of the β-Ti alloy specimen rolled by 1% (a) and the Gum Metal specimens rolled by 1% (b) and 10% (c–e). These images were taken at the same regions of the images in Fig. 3 with an electron beam direction parallel to ⟨1 1 1⟩.

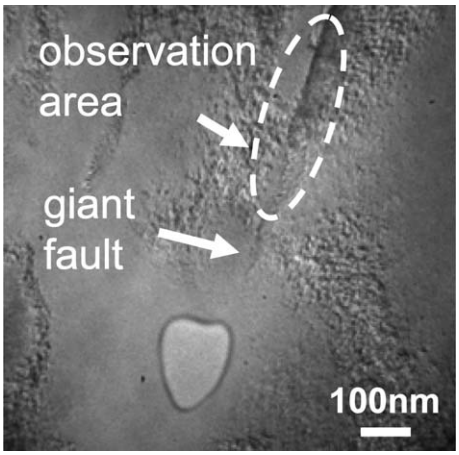

Fig. 5. TEM images of a cross-sectional observation of the Gum Metal specimen rolled by 10%. The image shows the thinned area in the vicinity of the giant fault by FIB in order to obtain a lattice image. The lattice image close to the giant fault was taken at the observation area. It is shown in Fig. 6.

the Gum Metal specimen rolled by 10% in Fig. 6 was taken at the area designated in Fig. 5. In this lattice image, a larger accumulation of local strain is found in the area close to the giant fault than in the images in Fig. 4. There are also many inhomogeneously distorted areas seen in Fig. 6(a) that are similar to those observed in Fig. 4. There is another feature: dipoles of partial dislocations can be observed as shown in the extended images in Figs. 6(b) and (c). These dipoles of partial dislocations can be formed by shears along $\langle 1\,1\,0\rangle\{1\,1\,0\}$. It is most remarkable that the formation of not only nanodisturbances but also dipoles of partial dislocations were observed. It is thought, from the first-principles calculations, that nanodisturbances can be formed in several directions, such as $\langle 1\,1\,0\rangle\{1\,1\,0\}$ and $\langle 1\,1\,1\rangle\{1\,1\,0\}$, $\{1\,1\,2\}$ or $\{1\,2\,3\}$, because they can be generated along elastically softened directions. We speculate that the nanodisturbances observed in the rolled Gum Metal specimens in Fig. 4 might be on $\langle 1\,1\,0\rangle\{1\,1\,0\}$. In the following sections, we examine theoretically the possibility of nanodisturbance generation along the elastically softened directions.

Finally, we note that the unique deformation behavior of Gum Metal at room temperature is hardly related to phase transformations. In particular, following experimental data [1–3,6], Gum Metal represents the 'pure' β-phase stable with respect to the omega phase. Furuta et al. [6] reported the β-phase stability of Gum Metal with the X-ray diffraction profile having only the β-phase peaks. Kuramoto et al. [3] observed the Gum Metal structure (after tensile deformation of about 10%) with only the β-phase in the giant fault vicinity. In this case, the diffraction patterns indicated only the presence of β-phase. Also, in Ref. [7] it was shown that an increase of the oxygen content in the β-phase of Ti–25V–1.0O alloy suppresses the formation of the omega phase. Because of the similarity between the compositions of this alloy and Gum Metal, the oxygen is expected to cause a similar 'stabilizing' effect in Gum Metal.

4. Nanodisturbances as dipoles of non-conventional partial dislocations

As has been well documented from HRTEM observations (see Section 3 and Refs. [1–3]), Gum Metal contains nanodisturbances that are planar nanoscopic areas of local shear. It is thought that such nanoscale imperfections play a crucial role in the formation of the unique mechanical properties of Gum Metal. In fact, they may be considered as carriers of the plastic deformation in Gum Metal, like the usual dislocations in conventional crystalline solids. Moreover, they look like partial dislocation dipoles in HRTEM images (see Figs. 1 and 6). The main differences between the nanodisturbances and 'normal' dislocation dipoles (dipoles of either perfect or partial lattice dislocations) are in their

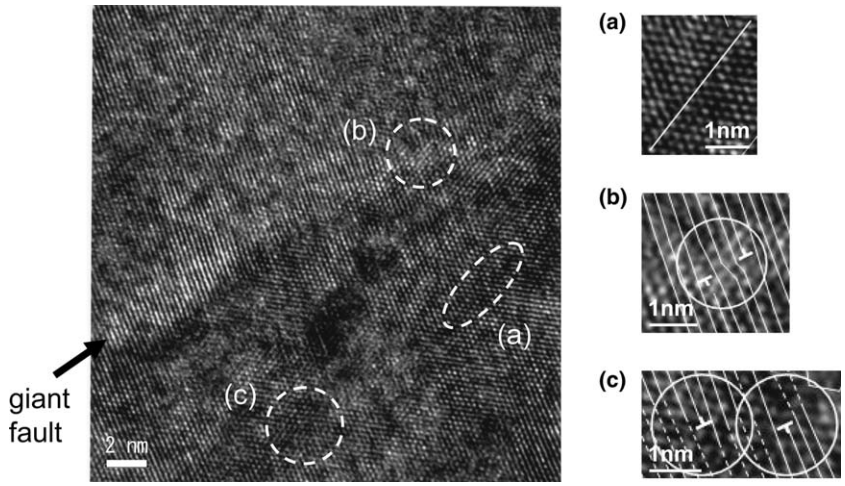

Fig. 6. High-resolution lattice images in the vicinity of the giant fault in the Gum Metal specimen rolled by 10%. This image was taken at the observation area designated and shown in Fig. 5 with an electron beam direction parallel to $\langle 1\,1\,1\rangle$. The extended image (a) indicates a nanodisturbance, while the images (b) and (c) show dipoles of partial dislocations.

characteristic Burgers vector magnitudes and their generation processes. We now discuss these differences.

The Burgers vector of a perfect lattice dislocation is the crystal lattice vector [8]. The Burgers vector of a partial lattice dislocation is a certain portion of the crystal lattice vector; it is strictly quantized by the crystallography of a material [8]. Nanodisturbances – planar nanoscopic areas of local plastic shear – are effectively modeled as dipoles of 'non-crystallographic' partial dislocations, i.e., dislocations with Burgers vectors having arbitrary, non-quantized magnitudes. In the most cases, the magnitudes of Burgers vectors of 'non-crystallographic' partial dislocations composing the nanodisturbances are smaller than the quantized magnitude of a Burgers vector of either a perfect or partial dislocation. Sometimes the magnitude of the Burgers vector of such 'non-crystallographic' partial dislocations becomes equal to that characterizing either a perfect or partial lattice dislocation. In these situations, the nanodisturbance transforms into a 'normal' dipole of (perfect or partial) lattice dislocations.

The differences in the generation of 'normal' dipoles of partial dislocations and that of nanodisturbances are schematically illustrated in Fig. 7. At the beginning of the homogeneous generation of a 'normal' dislocation dipole (Fig. 7(b)), the dislocations are located in close proximity to each other. The distance between them is around one crystal lattice parameter. Also, when a 'normal' dislocation dipole is generated (Figs. 7(b)–(d)), the dislocation Burgers vectors $\pm\boldsymbol{b}$ are constant during the nucleation process.

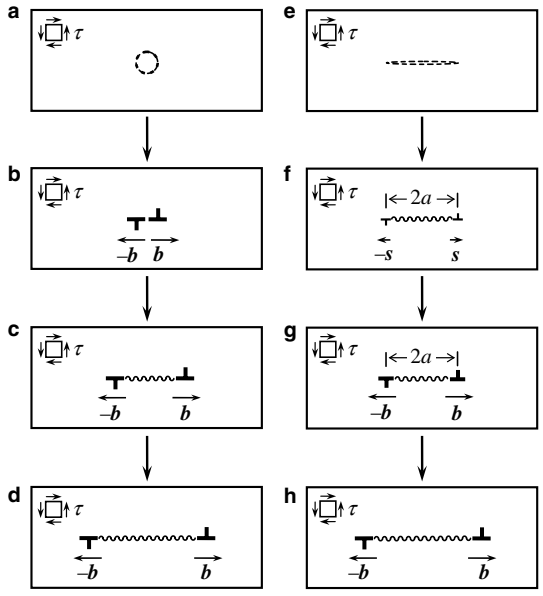

Fig. 7. Schematic representation of (a–d) homogeneous generation and extension of a dipole of partial edge dislocations with Burgers vectors $\pm\boldsymbol{b}$, and (e–h) homogeneous generation of an extended nanodisturbance in the form of a dipole of partial edge dislocations with a finite arm $2a$ and small Burgers vectors $\pm\boldsymbol{s}$ $(0 < s < b)$. When s increases and achieves the magnitude b, the nanodisturbance is transformed into a normal dipole of partial edge dislocations with Burgers vectors $\pm\boldsymbol{b}$, which can further extend under an external shear stress τ.

That is, the generation of a 'normal' dislocation dipole (Figs. 7(a)–(d)) occurs through the gradual increase (from 0) of the dipole arm $2a$ (the interdislocation spacing) at the constant Burgers vectors $\pm\boldsymbol{b}$ of the dislocations. Generation and evolution of a nanodisturbance are supposed to pass through two key stages (Figs. 7(e)–(h)). In the first stage, a nanodisturbance is generated as a result of a local momentary ideal shear (Figs. 7(e) and (f)) at a nanoscale area. That is, the momentary ideal shear produces a planar nanodisturbance with a finite nanoscopic length $2a$ equal to some (from about 5 to 20) crystal lattice parameters. At the beginning of its generation (Figs. 7(e) and (f)), the nanodisturbance represents a dipole of 'non-crystallographic' partial dislocations distanced by a finite nanoscopic length $2a$ and characterized by the non-quantized ('non-crystallographic') Burgers vectors $\pm\boldsymbol{s}$ with quite small magnitude $s \ll b$, where $s = |\boldsymbol{s}|$ and $b = |\boldsymbol{b}|$. The Burgers vector magnitude s increases under a shear stress τ (occurring due to external and/or internal sources) and finally becomes equal to b; see Fig. 7(g). (The nanodisturbance length may be constant or not during this process.) In the second stage, when $s = b$, the nanodisturbance is transformed into a 'normal' dipole of partial dislocations that may extend further under the action of τ (Figs. 7(g) and (h)).

With the experimental data reported in Section 3 and Refs. [1–3], nanodisturbances represent typical structural elements of deformed Gum Metal and so are expected to contribute to its plastic flow. In this case, the homogeneous generation of nanodisturbances (Figs. 7(e)–(h)) in mechanically loaded Gum Metal should effectively compete with both the homogeneous generation of normal dislocation dipoles (Figs. 7(a)–(d)) and the conventional deformation mechanism by the movement of pre-existing lattice dislocations. Experiments [1,2] show that conventional dislocation activity is not essential in Gum Metal. Movement of pre-existing lattice dislocations can be effectively suppressed by atmospheres (like Cottrell ones) of inhomogeneously distributed solutes in Gum Metal. According to the theory of point defects in strained alloys [9,10], such atmospheres are formed (after some time interval depending on the diffusivity of solutes) near dislocations, because of the interaction between solutes and elastic stresses created by dislocations. Also, there can be local interactions between solute atoms and lattice dislocation cores, the dislocation lines where the ideal crystal lattice is violated. There may be special sites in the dislocation core that more easily accommodate solutes, leading to a binding energy of solutes to the core. These effects limit the lattice dislocation mobility.

Thus, the pre-existing lattice dislocations are immobile in Gum Metal and do not contribute to plastic flow, because solute atmospheres limit the dislocation mobility. In contrast, the mobility of as-generated lattice dislocation dipoles and nanodisturbances (Fig. 7) is not suppressed by the atmospheres whose formation is a slow process controlled by diffusion of solutes. Therefore, the as-generated lattice dislocation dipoles and nanodisturbances are mobile

enough (in contrast to the pre-existing lattice dislocations) to effectively carry plastic flow in Gum Metal. In the context discussed, it is important to investigate which scenario, as shown in Figs. 7(a)–(d) or 7(e)–(h), is more realistic in deformed Gum Metal. In Sections 5 and 6, we do this by estimating and comparing the conditions for homogeneous generation of nanodisturbances and that of dipoles of conventional partial dislocations.

5. Generation of dipoles of conventional partial dislocations: Energy characteristics

First, consider the homogeneous generation of a dipole of conventional partial edge dislocations with Burgers vectors $\pm\boldsymbol{b}$ in an infinite elastically isotropic solid under the action of an external shear stress τ. The total energy of the system (per unit dislocation length) is changed by the value $\Delta W_{\rm dip}$:

$$\Delta W_{\rm dip} = W^{\rm e}_{\rm dip} + W^{\rm c}_{\rm dip} + W^{\gamma}_{\rm dip} - A_{\rm dip} \tag{1}$$

where $W^{\rm e}_{\rm dip}$ is the strain energy of the dipole, $W^{\rm c}_{\rm dip}$ is its core energy, $W^{\gamma}_{\rm dip}$ is the energy of the stacking fault strip between the partial dislocations of the dipole, and $A_{\rm dip}$ is the work spent by the shear stress τ to generate the dipole. All of these terms are well known (see, for instance, Refs. [8,11]) and are determined by the following equations:

$$W^{\rm e}_{\rm dip} = Db^2 \ln\frac{2a - r_{\rm c}}{r_{\rm c}}, \quad W^{\rm c}_{\rm dip} = Db^2 Z,$$
$$W^{\gamma}_{\rm dip} = 2a\gamma, \quad A_{\rm dip} = 2ab\tau \tag{2}$$

where $D = G/[2\pi(1-\nu)]$ (where G is the shear modulus and ν the Poisson ratio), b is the magnitude of the Burgers vector of a partial dislocation, $2a$ is the dipole arm, $r_{\rm c}$ is the cut-off radius of the dislocation elastic fields at the dislocation core, Z is a parameter characterizing the dislocation core energy and γ is the stacking fault energy (per unit square). For simplicity we take $r_{\rm c} \approx b$ and $Z \approx 1$. We also introduce the dimensionless normalized dipole arm $x = 2a/b$. Taking this into account, the energy change (Eq. (1)) is written as

$$\Delta W_{\rm dip} = Db^2\left[\ln(x-1) + 1 + x\frac{\gamma - \tau b}{Db}\right] \tag{3}$$

When $\gamma/b \geqslant \tau$, the function $\Delta W_{\rm dip}(x)$, $x > 1$, is always positive and grows monotonically. In this case, the homogeneous generation of the dipole is impossible, which is illustrated by curve 1 in Fig. 8, where the function $\Delta W_{\rm dip}(x)$ is plotted for various values of τ, with the standard approximation $\gamma \approx DB\kappa$. Here, B ($\approx 2b$) is the Burgers vector magnitude of a perfect dislocation and κ ($\ll 1$) is a dimensionless parameter. The plots in Fig. 8 are given at $\kappa = 0.01$.

If $\gamma/b < \tau$ and τ is not very large, the function $\Delta W_{\rm dip}(x)$ is first positive and achieves its maximum, and then monotonically decreases (curves 2–4 in Fig. 8). The maximum value $\Delta W^{\rm max}_{\rm dip} = \Delta W_{\rm dip}(x = x_{\rm c})$ is the energy barrier for the dipole generation, and the normalized dipole arm x takes its critical value $x_{\rm c}$ for the given stress τ. The physical meaning of the critical dipole arm $x_{\rm c}$ is that the dipole with a smaller arm, if it appears, cannot exist and must annihilate, while that with a larger arm, if it appears, can exist and must increase its arm. As follows from Fig. 8, the energy barrier $\Delta W^{\rm max}_{\rm dip}/(Db^2)$ takes values of about 2.5, 1 and 0.3 for stress values $\tau/D = 0.1$, 0.3 and 0.5, respectively. With the characteristic values of $G \approx 9$ GPa [3], $\nu = 0.3$ and $b = 0.145$ nm, which are close to typical data for Gum Metal, we obtain $\Delta W^{\rm max}_{\rm dip} \approx 0.67$, 0.27 and 0.08 eV/nm at $\tau = 0.2$, 0.6 and 1 GPa, respectively. Let us compare these values of $\Delta W^{\rm max}_{\rm dip}$ with typical values of a thermal fluctuation $nk_{\rm B}T$ (where $n \approx 4$ is the number of atoms per nanometer, $k_{\rm B}$ is the Boltzmann constant and T is the absolute temperature). For $T = 300$ K, we have $nk_{\rm B}T \approx 0.1$ eV/nm. The probability P of a thermal fluctuation equal to the value of $\Delta W^{\rm max}_{\rm dip}$ is determined by the standard formula: $P = \exp(-\Delta W^{\rm max}_{\rm dip}/nk_{\rm B}T)$. Therefore, the probabilities of thermal fluctuations equal to energies of 0.67, 0.27 and 0.08 eV/nm are estimated by the values of about 0.001, 0.1 and 0.46. The last two values are high enough to expect the homogeneous nucleation of partial dislocation dipoles at room temperature under the stress values of $\tau \geqslant 0.6$ GPa.

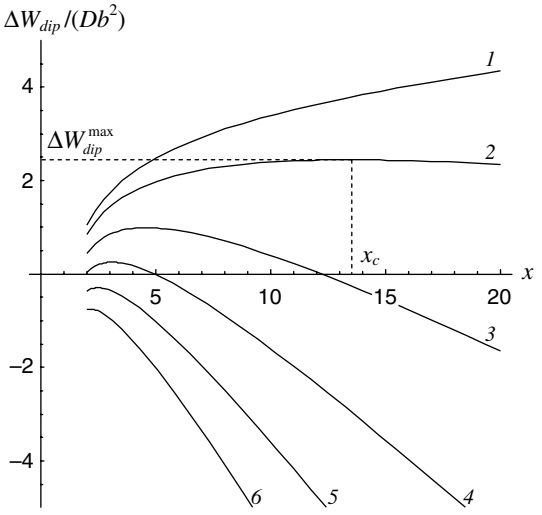

Fig. 8. Dependence of the energy change $\Delta W_{\rm dip}$ due to homogeneous generation of a dipole of partial dislocations on its normalized arm $x = 2a/b$. The external stress values are $\tau/D = 0$ (curve 1), 0.1 (curve 2), 0.3 (curve 3), 0.5 (curve 4), 0.7 (curve 5) and 0.9 (curve 6). The stacking fault energy is approximated by the formula $\gamma \approx DB\kappa$ with $\kappa = 0.01$.

When $\gamma/b < \tau$ and τ is very large, the function $\Delta W_{\rm dip}(x)$, $x > 1$, is always negative and decreasing (curve 6 in Fig. 8). This case corresponds to barrierless generation of the dislocation dipole. However, it is characterized by unrealistically high values of $\tau \approx D \approx G/4$. Therefore, below we consider only the case of barrier generation and find the dependence of the critical arm $x_{\rm c}$ on the stress τ. Taking the partial derivative and putting it equal to zero

$$\frac{\partial \Delta W_{\rm dip}}{\partial x} = Db^2\left(\frac{1}{x-1} + \frac{\gamma - \tau b}{Db}\right) = 0 \tag{4}$$

we find the critical dipole arm

$$x_c = 1 + \frac{Db}{\tau b - \gamma} \tag{5}$$

With the approximation $\gamma \approx DB\kappa$, this equation may be rewritten in the following form:

$$x_c = 1 + \frac{1}{\tau/D - \kappa B/b} \tag{6}$$

6. Generation of nanodisturbances, dipoles of non-conventional partial dislocations: Energy characteristics

Consider now a similar situation with homogeneous generation of a two-dimensional nanodisturbance (Figs. 7(e)–(h)). To calculate the energy characteristics of its generation, we describe the nanodisturbance as a dipole of non-conventional partial dislocations; that is, edge partial dislocations with small Burgers vectors $\pm\boldsymbol{s}$, whose non-quantized magnitude lies within the interval $0 < s < B$.

When such a model imperfection is generated under an external shear stress τ, the total energy of the system (per unit dislocation length) is changed by the value ΔW_{nd}:

$$\Delta W_{nd} = W^{e}_{nd} + W^{\gamma}_{nd} - A_{nd} \tag{7}$$

where W^{e}_{nd} is the strain energy of the nanodisturbance, W^{γ}_{nd} is the energy of the stacking fault strip between its edges and A_{nd} is the work spent by the shear stress τ to generate the nanodisturbance. The first term in Eq. (7) is similar to that in Eq. (1), with replacement of b and r_c by s:

$$W^{e}_{nd} = Ds^2 \ln\frac{2a - s}{s} \tag{8}$$

where $2a$ is now the size of the nanodisturbance.

In the situation under discussion, the stacking fault energy W^{γ}_{nd} consists of two terms. The first term corresponds to the energy of the stacking fault fragment of length $(2a - s)$, while the second term describes the energy of the stacking faults at the two edge fragments each having the length s. When the nanodisturbance is transformed into a dipole of perfect dislocations, the first term becomes equal to zero, while the second term transforms into the energy of two cores of the perfect lattice dislocations composing the dipole. In the framework of the model suggested, these two terms are approximated by periodic functions of s in the range from 0 to B. In this approximation, the first function reaches its maximum at $s = B/2$; that is, when the displacement mismatch between the atomic layers adjacent to the stacking fault reaches its maximum. The second function reaches its maximum at $s = B$; that is, when the dipole of perfect dislocations is completely generated. In these circumstances, the stacking fault energy W^{γ}_{nd} is effectively approximated by

$$W^{\gamma}_{nd} = \gamma(2a - s)\sin\frac{\pi s}{B} + Ds^2 \sin\frac{\pi s}{2B} \tag{9}$$

The work A_{nd} is given by

$$A_{nd} = 2as\tau \tag{10}$$

As a result, Eq. (7) may be rewritten as follows:

$$\Delta W_{nd} = Db^2\left[p^2 \ln\frac{x - p}{p} + (x - p)\frac{\gamma}{Db}\sin\frac{\pi p}{B/b} + p^2 \sin\frac{\pi p}{2B/b} - xp\frac{\tau}{D}\right] \tag{11}$$

where $p = s/b$. Qualitatively, the behavior of the function $\Delta W_{nd}(x)$ is similar to that of the function $\Delta W_{dip}(x)$. Plots of $\Delta W_{nd}(x)$ are shown in Fig. 9 for three values of the ratio $p = 0.1$ (Fig. 9(a)), 0.5 (Fig. 9(b)) and 0.9 (Fig. 9(c)), and different values of the stress τ. As follows from Fig. 9, when τ is very small (curve 1), $\Delta W_{nd}(x)$ is always positive and increasing. In this case, we cannot expect homogeneous generation of such nanodisturbances.

For larger levels of τ (curve 2 in Fig. 9(a), curves 2–4 in Figs. 9(b) and (c)), there exist energy barriers ΔW^{max}_{nd} whose heights strongly depend on p and τ. For example, the same levels of τ ($\tau/D = 0.1$, 0.3 and 0.5, or $\tau = 0.2$, 0.6 and 1 GPa, respectively), which we considered in Section 5, here give (for $x \geqslant 2$) $\Delta W^{max}_{nd}/(Db^2) \approx 0.5$, 0.1 and 0 at $p = 0.5$, and 1.7, 0.5 and 0.05 at $p = 0.9$, respectively. These values are notably smaller than those characterizing homogeneous generation of a 'normal' dipole of partial dislocations (about 2.5, 1 and 0.3, respectively, see Section 5). With the characteristic values $G \approx 9$ GPa [3], $\nu = 0.3$ and $b = 0.145$ nm, close to the typical parameters of Gum Metal, for $\tau = 0.2$, 0.6 and 1 GPa, we obtain the following estimates: $\Delta W^{max}_{nd} \approx 0.135$, 0.027 and 0 eV/nm at $p = 0.5$, and 0.459, 0.135 and 0.0135 eV/nm at $p = 0.9$, respectively. At room temperature, $T = 300$ K, the probabilities of thermal fluctuations (see Section 5) equal to these energy values are approximately 0.26, 0.76 and 1 at $p = 0.5$, and 0.01, 0.26 and 0.87 at $p = 0.9$, respectively. These estimates are much higher than those (0.001, 0.1 and 0.46, respectively) obtained in Section 5 for dislocation dipoles.

Note that the above estimates are done for the interval $x \geqslant 2$ just to compare the energy barriers for generation of dislocation dipoles and nanodisturbances. However, as we have previously detailed, nanodisturbances are generated by a nanoscale ideal shear. In this case, as-generated nanodisturbances have nanoscopic length values (Fig. 7(f)), essentially exceeding the lattice parameter. Therefore, one needs to analyze the interval $x \gg 2$, where the energy barriers are small or even absent (Fig. 9). Thus, the above estimates for the energy barriers may be viewed as the upper limits, while those for the probabilities are the lower ones.

When τ is very large, the function $\Delta W_{nd}(x)$, $x > 1$, is always negative and decreasing (curves 3–6 in Fig. 9(a), curves 5 and 6 in Figs. 9(b) and (c)). This case corresponds to barrierless generation of the nanodisturbance, and the value of τ needed depends on the ratio p ($\tau \approx 0.3D \approx G/13$ at $p = 0.1$ and $\tau \approx 0.7D \approx G/6$ at $p = 0.5, \ldots, 0.9$). These levels of τ are also smaller than those for barrierless generation of dislocation dipoles (see Section 5).

We return to the case of barrier generation and ascertain the dependence of the critical length x_c of the nanodis-

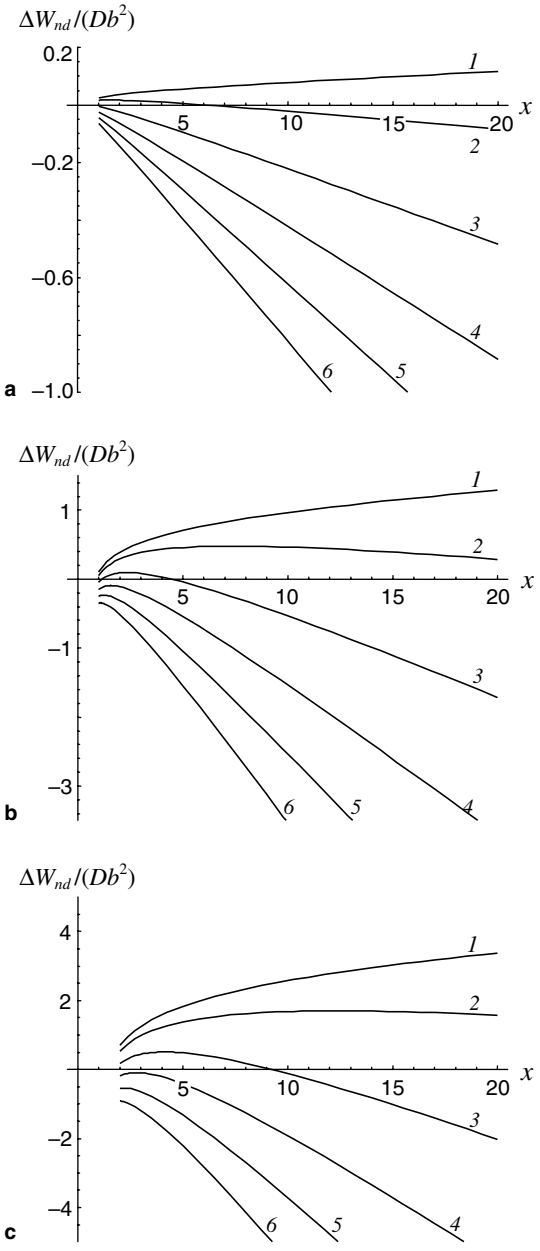

Fig. 9. Dependence of the energy change $\Delta W_{\rm nd}$ due to homogeneous generation of a nanodisturbance on its normalized length $x = 2a/b$. The normalized magnitude of its Burgers vector $p = s/b$ is equal to (a) 0.1, (b) 0.5 and (c) 0.9. The external stress values are $\tau/D = 0$ (curve 1), 0.1 (curve 2), 0.3 (curve 3), 0.5 (curve 4), 0.7 (curve 5) and 0.9 (curve 6).

turbance (which corresponds to the energy barrier $\Delta W_{\rm nd}(x = x_{\rm c}) = \Delta W_{\rm nd}^{\max}$) on the stress τ. The partial derivative of $\Delta W_{\rm nd}(x)$ with respect to x is given by

$$\frac{\partial \Delta W_{\rm nd}}{\partial x} = Db^2\left(\frac{p^2}{x-p} + \frac{\gamma}{Db}\sin\frac{\pi p}{B/b} - p\frac{\tau}{D}\right) \tag{12}$$

The critical size $x_{\rm c}$ of the nanodisturbance is then determined from the equation

$$\left.\frac{\partial \Delta W_{\rm nd}}{\partial x}\right|_{x=x_{\rm c}} = 0 \tag{13}$$

which finally gives

$$x_{\rm c} = p\left(1 + \frac{p}{\frac{\tau}{D}p - \frac{B\kappa}{b}\sin\frac{\pi p}{B/b}}\right) \tag{14}$$

where the approximation $\gamma \approx DB\kappa$ has been used. For $p \ll 1$, this formula results in

$$x_{\rm c} = p\left(1 + \frac{1}{\tau/D - \kappa\pi}\right) \tag{15}$$

In comparing Eqs. (6) and (15), one can see that they differ mainly by the factor $p \ll 1$ (the ratio $B/b \approx 2$ is of the same order as π). Therefore, the critical size of a weak (with a small p) nanodisturbance is much smaller than the critical arm of a partial dislocation dipole for the same level of the external shear stress τ. When $p = 1$ (i.e., the nanodisturbance is transformed into a dipole of partial dislocations), Eq. (14) is reduced to Eq. (6). The case of arbitrary p is illustrated in Fig. 10.

One can conclude that for a given level of the external shear stress τ, the critical size of a nanodisturbance is significantly smaller than the critical arm of a dipole of partial dislocations. Weak nanodisturbances can easily be generated at relatively small values of τ. Thus, if homogeneous generation of nanodisturbances occurs in Gum Metal, it must prevail over the generation of 'unfavored' dipoles of partial dislocations. The principal factor causing nanodisturbances to be predominant over ordinary dislocations in Gum Metal is related to the intrinsic elastic anomaly. Gum Metal can attain a very small ideal strength and thereby contain nanodisturbances, because the elastic anomaly makes the shear moduli of $\langle 1\,1\,0\rangle\{1\,1\,0\}$ and $\langle 1\,1\,1\rangle\{1\,1\,0\}$, $\{1\,1\,2\}$ or $\{1\,2\,3\}$ very small, i.e., the values of τ and D are of the same order of magnitude.

Note that nanodisturbances may appear in non-crystallographic planes where 'normal' dislocation dipoles are not generated due to their large Burgers vector magnitudes (b)

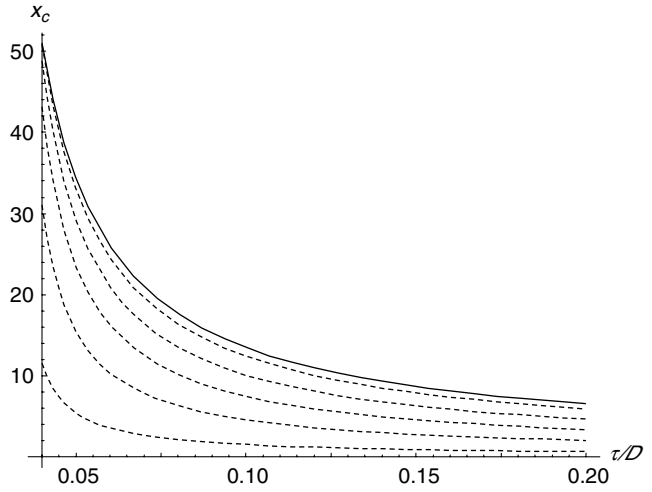

Fig. 10. Critical dipole arm (solid line) or nanodisturbance length (dashed lines) $x_{\rm c}$ vs. the external shear stress τ. The dashed curves are plotted for the normalized relative displacement $p = 0.1$, 0.3, 0.5, 0.7 and 0.9, from bottom to top, respectively.

and corresponding low probability $\sim\exp(-\alpha b^2)$ of dislocation generation. The presence of such nanodisturbances lying in 'abnormal' planes is supported by direct HRTEM observations (see Section 3). This is explained by the fact that they appear, as there are no limitations on their strength s, which may be very small. In this situation, the homogeneous generation of nanodisturbances, the increase of their strength and their further extension represent a specific and very effective mechanism for plastic deformation in Gum Metal.

7. Discussion and concluding remarks

Our experimental HRTEM analysis (see Section 3) has shown that nanodisturbances – planar nanoscopic areas of local shear – are typical elements of the defect structure in deformed Gum Metal. Nanodisturbances are effectively modeled as dipoles of non-conventional partial dislocations with arbitrary, non-quantized Burgers vectors (see Sections 4 and 6). These nanoscale defects are different from dipoles of conventional perfect or partial dislocations in crystal lattices, and their occurrence is due to the low resistance to shear in certain crystallographic planes of Gum Metal. In the context discussed, the nanodisturbances represent a new type of defects in solids. Following the results of the theoretical analysis given in Section 6, the homogeneous generation of nanodisturbances is energetically favorable in Gum Metal where they serve as effective carriers of plastic flow. The homogeneous generation of nanodisturbances, the increase of their strength (Burgers vector magnitude) and their further extension (Figs. 7(e)–(h)) represent a specific and very effective mechanism for plastic deformation in Gum Metal.

The deformation mechanism with nanodisturbances carrying plastic flow is in competition with the conventional dislocation slip that is dominant in most crystalline metals. However, conventional dislocation slip can be effectively suppressed in Gum Metal due to both the effects of solute atmospheres on the mobility of pre-existing conventional dislocations in Gum Metal (for details, see the discussion in Section 4) and the large energetic barriers for the homogeneous generation of conventional dislocation dipoles (see Section 5).

Besides nanodisturbances, giant faults – planar macroscopic areas in which very large plastic strain is localized – have been experimentally observed in Gum Metal (see Section 3 and Refs. [1–3]). From the results of our experimental and theoretical studies reported in this paper, the formation of giant faults can be related to the evolution of nanodisturbances in deformed Gum Metal as follows. Nanodisturbances are intensively generated in Gum Metal at the first stage of deformation. When their density becomes high, the elastic interaction between the nanodisturbances becomes relevant and provides for the softening of Gum Metal where they carry plastic flow. The softening causes plastic strain instability in Gum Metal with very large plastic flow being localized in giant faults. This, however, is just a qualitative scenario whose detailed analysis is to be published elsewhere.

Thus, with the results of both our experimental data and theoretical analysis, Gum Metal with a low resistance to shear in certain crystallographic planes is found to be deformed by the specific deformation mechanism with nanodisturbances carrying plastic flow. We have demonstrated that this deformation mechanism is intrinsic to Gum Metal. In general, the deformation mechanism associated with nanodisturbances can operate in materials other than Gum Metal. In particular, we think that nanodisturbances can contribute to superplastic deformation in nanocrystalline materials in which grain boundaries are commonly characterized by low resistance to shear [12–17]. For instance, intergrain sliding – a relative shear of neighboring grains that is localized in the boundary between grains – is the dominant deformation mode in nanocrystalline materials showing superplasticity [12,13] and essentially contributes to plastic deformation of ductile nanocrystalline metals [14,15]. Intergrain sliding in high-angle grain boundaries occurs through either local shear events [18–21] or movements of grain boundary dislocations [11,18,22,23]. In particular, basic carriers of the intergrain sliding in disordered grain boundaries are treated to be free-volume defects, nanometer-size spheroidal regions where, due to the presence of an extra free volume, the shear resistance is less than in the rest of the grain boundary [18–21]. Ensembles of such free-volume defects homogeneously distributed in the grain boundary phase provide local shear events as elementary acts of intergrain sliding. Though a reported approach [18–21] has shed light on deformation conducted by grain boundaries, it gives no clear interpretation of local shear events in terms of defects (as the stress sources in solids) which is highly desirable for an adequate description of the intergrain sliding and its contribution to plastic flow. In the spirit of the approach developed in this paper, the local shear events in grain boundaries can be effectively modeled as the events involving the generation of three-dimensional nanodisturbances (that is, nanoscale loops of non-conventional partial dislocations with non-quantized Burgers vectors). The role of nanodisturbances in plastic deformation processes in nanocrystalline materials, and the unique properties of Gum Metal will be the subject of further investigations by us.

Acknowledgments

This work was supported in part (for M.Yu.G. and I.A.O.) by a Research Agreement with Toyota Central R&D Laboratories. The authors are grateful to Dr. Chihiro Iwamoto of Kumamoto University and Dr. Kayo Horibuchi of Toyota Central R&D Laboratories for their assistance in the TEM observations and to Dr. Takashi Saito, Tadahiko Furuta, Dr. Jung-Hwan Hwang, Dr. Kazuaki Nishino, Hideaki Ikehata and Naoyuki Nagasako of Toyota Central R&D Laboratories for discussions.

References

[1] Saito T, Furuta T, Hwang J-H, Kuramoto S, Nishino K, Suzuki N, et al. Science 2003;300:464.
[2] Saito T, Furuta T, Hwang J-H, Kuramoto S, Nishino K, Suzuki N, et al. Mater Sci Forum 2003;426:681.
[3] Kuramoto S, Furuta T, Hwang J-H, Nishino K, Saito T. Metall Mater Trans A [in press].
[4] Ikehata H, Nagasako N, Furuta T, Fukumoto A, Miwa K, Saito T. Phys Rev B 2004;70:174113.
[5] Krenn CR, Roundy D, Morris JW, Cohen ML. Mater Sci Eng A 2001;319:111.
[6] Furuta T, Kuramoto S, Hwang J-H, Nishino K, Saito T. Mater Trans 2005;46:3001.
[7] Williams JC, Hickman BS, Leslie DH. Metall Trans 1971;2:477.
[8] Hirth JP, Lothe J. Theory of dislocations. New York (NY): Wiley; 1982.
[9] Girifalco LA, Welch DO. Point defects and diffusion in strained metals. New York: Gordon and Breach; 1967.
[10] Teodosiu C. Elastic models of crystal defects. Berlin/Heidelberg/New York (NY): Springer; 1982.
[11] Gutkin MYu, Ovid'ko IA. Plastic deformation in nanocrystalline materials. Berlin/Heidelberg/New York (NY): Springer; 2004.
[12] Mukherjee AK. Mater Sci Eng A 2002;322:1.
[13] Zhan G-D, Kuntz JD, Wan J, Mukherjee AK. MRS Symp Proc 2003;740:41.
[14] Kumar KS, Suresh S, Chisholm MF, Horton JA, Wang P. Acta Mater 2003;51:387.
[15] Kumar KS, Suresh S, Van Swygenhoven H. Acta Mater 2003;51:5743.
[16] Pilling J, Ridle N. Superplasticity in crystalline solids. London: Institute of Metals; 1989.
[17] Ruano OA, Wadsworth J, Sherby OD. Acta Mater 2003;51:3634.
[18] Sutton AP, Balluffi RW. Interfaces in crystalline materials. Oxford: Oxford Science Publications; 1996.
[19] Conrad H, Narayan J. Scr Mater 2000;42:1025.
[20] Van Swygenhoven H, Derlet PM. Phys Rev B 2001;64:224105.
[21] Padmanabhan KA, Gleiter H. Mater Sci Eng A 2004;381:28.
[22] Gutkin MYu, Ovid'ko IA, Skiba NV. Acta Mater 2003;51:4059; Gutkin MYu, Ovid'ko IA, Skiba NV. Acta Mater 2004;52:1711.
[23] Ovid'ko IA. Int Mater Rev 2005;50:65.